QUANTITATIVE ASSESSMENT OF SALT DISTRIBUTION IN POROUS MEDIA

Fatima-Zohra Sahraoui[1†], Mykyta V. Chubynsky[2], Nihal Muhammed Habeeb[2], Ran Holtzman[2], Pascale Sénéchal[3], Hannelore Derluyn[4], David Thickett[5], Haida Liang[1] and Lucas Goehring[1*]

Abstract

Many cultural heritage sites suffer from damage induced by salt crystallization in natural materials such as sandstone, both on its surface and interior. Key questions in predicting and mitigating damage due to salt remain open due to the complex interactions between the transport of salts with moisture in the interior of such materials, and the salt precipitation that can itself affect further transport. To understand when and where salt precipitates in porous materials, this project combines accelerated weathering experiments, high-resolution X-ray tomography imaging (micro-CT) and numerical simulations, where detailed experimental data serve to help formulate a computationally efficient pore-network model. By considering the controlling factors, including the pore distribution of the material and environmental conditions, this model aims to provide a novel method to predict and design remediation of salt damage in cultural heritage applications.

Keywords: Salt deterioration, laboratory investigation, X-ray micro-computed tomography, pore-network model.

1 Introduction

Salts are a significant contributor to deterioration in historic buildings. Traditional building materials like sandstone, marble, concrete, brick and mortar are porous, and soluble salts can leech from their mineral composition, arise from chemical alteration and weathering, or enter from external sources like groundwater or aerosols (Flatt *et al.* 2014; 2017). Among the various salts commonly encountered in conservation scenarios, sodium sulfate presents a particular challenge, due to its complex polymorphic nature (Flatt *et al.* 2017; Lubelli *et al.* 2018). This salt exists in two extreme forms, mirabilite ($Na_2SO_4 \cdot 10H_2O$) and thenardite (Na_2SO_4), along with intermediate hydration states. The transitions between these phases are sensitive to climatic fluctuations, and especially to relative humidity and temperature variations, complicating prediction and management (Nunes *et al.*, 2021). These phase transitions also result in significant volume expansion, over 300%, generating mechanical stress that contributes to material decay (Flatt *et al.* 2014).

Whatever their origin, salts are easily transported along with any available water but will crystallise within the porous structure of building materials whenever their concentration exceeds some solubility limit. At this point the salts will either precipitate into a solid that clogs up the pores of the material, a phenomenon known as *subflorescence,* or will contribute to the growth of a salt deposit at the surface, visible as salt *efflorescence*. The precipitation of salts at the pore scale is a complex process, and is influenced by properties like porosity, pore geometry, and environmental conditions (Lubelli *et al.* 2018; Nunes *et al.* 2021). Salts can precipitate in different locations, within the pores themselves, or within connecting throats, and the pattern of their formation impacts further fluid transport and precipitation pathways within the pore network (Wetzei *et al.* 2020). This feedback between fluid flow and the alteration of transport properties is an example of *reactive transport* in porous media, the more general understanding of which represents an important open challenge for a wide range of geophysical and engineering applications (Seigneur *et al.* 2019; Noriel and Soulaine 2021).

To predict salt crystallisation behaviour, thermodynamic models like ECOS/RUNSALT are extensively employed (Menéndez 2017; Godts *et al.* 2022). These models allow prediction of the equilibrium crystallisation behaviour of salt mixtures under varying environmental conditions. Nevertheless, they neglect constraints related to salt transport mechanisms and pore-scale precipitation processes, including the dynamics of supersaturation. Addressing these gaps is critical to improving predictions of salt kinetics and related deterioration in heritage materials (Godts *et al.* 2024).

Micro-computed X-ray tomography (micro-CT) has emerged as a useful non-invasive imaging technique available to heritage research. It significantly advances the capability to visualise and quantify salt precipitation in 3D volumes (Li *et al.* 2024); can be used to characterise the internal physical properties of heritage materials, such as their pore structure, and the internal damage resulting from salt crystallisation (Reedy and Reedy 2022); and can capture porosity evolution during fluid imbibition and precipitation phenomena (Miletić *et al.* 2024). These applications highlight the advantages of

[1] School of Science and Technology, Nottingham Trent University, Nottingham NG11 8NS, United Kingdom

[2] Centre for Fluid and Complex Systems, Coventry University, Coventry CV1 5FB, United Kingdom

[3] Université de Pau et des Pays de l'Adour, E2S UPPA, CNRS, DMEX, Pau, France

[4] Université de Pau et des Pays de l'Adour, E2S UPPA, CNRS, LFCR, Pau, France

[5] English Heritage, Rangers House, Chesterfield Walk, London SE10 8QX, United Kingdom

†fatima-zohra.sahraoui2022@my.ntu.ac.uk *lucas.goehring@ntu.ac.uk

micro-CT over destructive sampling methods, such as in providing insights into the extraction of model parameters, or in the assessment of salt deposits in subsurface accumulations that might remain undetectable by other methodologies.

Despite these benefits, accurately imaging salts using micro-CT involves significant challenges. Salts often exhibit similar X-ray characteristics to the surrounding matrix, complicating their differentiation from other phases. Laboratory micro-CT systems also face resolution limitations and are often insufficient to adequately resolve nanopores and thin salt films, potentially underestimating salt content and crystallisation effects (Analytical Methods Committee 2021). Faced with similar limitations in other imaging methods, researchers have employed advanced segmentation methods, including machine learning and deep convolutional neural networks, to enhance segmentation accuracy (Kogou *et al.* 2025).

Building upon these advances, this work introduces and applies a comprehensive, reproducible micro-CT imaging protocol to investigate sodium sulfate crystallisation patterns within sandstone analogues made from glass beads. By controlling the physical parameters of this artificial sandstone, the surrounding environmental conditions, and the nature of the invading salt, we aim to assess salt distributions at the pore scale, and to improve understanding of the impact of salt deposits on fluid and moisture transport. The sample dimensions are selected to remain representative of larger-scale scenarios, while still maintaining sufficient spatial resolution to confidently capture the crystallisation patterns within pores. The micro-CT scanning parameters are optimised to minimise image artifacts and to offer the best contrast between the salt crystals, matrix grains, and air-filled pores. Advanced machine-learning-based segmentation techniques are then deployed for accurately detecting sodium sulfate crystals within stone-like materials.

Our approach to evaluating salt precipitation aims to provide a foundation for computational models that simulate salt transport and damage propagation in historic stone materials. Specifically, we outline here a dynamic pore-network model (PNM) that can predict the transport of salt through a porous material like stone. In a PNM, the pore geometry is discretised into an interconnected network of pores connected by throats (constrictions). Physically-based constitutive relations describe the transport properties of this network and predict properties such as fluid and salt content, capillary pressure and vapour pressure. This approach can provide a sample-scale description at a fraction of the computational resources required for other pore-scale models (Zhao *et al.* 2019). We present preliminary results from this model and compare its predictions of the pattern of salt deposition in a drying porous stone with corresponding experiments imaged by micro-CT. This combination of experimental and computational techniques enables a quantitative assessment of salt damage processes and supports the development of predictive tools for long-term heritage material preservation.

2 Experimental methods

This study focuses on the transport of salt in analogues of natural building materials, like sandstone, to better understand the potential damage that salt migration and crystallisation poses to historic buildings. To this end, we made cylindrical samples out of cohesive glass beads, soaked them in solutions of sodium sulfate, dried them under controlled environmental conditions, and then scanned them using micro-computed X-ray tomography (micro-CT). The experiments were designed to mimic different degrees of salt impregnation in building materials, and to evaluate the influence of salt content on the nucleation and growth patterns within the pore spaces (subflorescence) and sample surface (efflorescence).

2.1 Drying experiments

Samples of artificial sandstone were prepared using a recipe adapted from Hemmerle *et al.* (2016). Glass beads (200–300 µm diameter) were mixed with PVA glue (ABEEC) in a 3:97 wt.% ratio, compacted into cylindrical holders (5 cm height × 5 cm diameter) and left to cure. Once set, samples were partially sealed by wrapping their circumference with parafilm. They were then saturated by capillary rise with sodium sulfate (Sigma, anhydrous Na_2SO_4) solutions, at concentrations of 0.59 M, 1.19 M and 1.78 M, which are 30%, 60%, and 90% of the solubility of Na_2SO_4 at 20°C. For this, specimens were immersed to a depth of 1 cm in the solution, allowing for imbibition of liquid through the cylinder, and a uniform initial distribution of salt and water. The upper face of each cylinder was left open, to permit evaporation, and the samples were left to dry under ambient conditions (16–19°C, 30–50% RH). A typical, fully dried specimen is shown in Fig. 1(a).

2.2 Micro-computed tomography

High-resolution X-ray tomograms of dried, salt-contaminated samples were acquired with a TESCAN UniTOM XL Micro-CT scanner at DMEX-UPPA (FRANCE). Settings were chosen to optimize the contrast between the air, beads and salt, while minimising imaging artifacts. Samples were mounted vertically and perpendicular to the beam axis to preserve structural orientation and reduce rotational misalignment during scanning. Full-volume scans had 30 µm voxel resolution with scanning parameters of 120 kV, 30 W and exposure time 80 ms, while smaller volumes near the sample surface were imaged with 10 µm resolution with scanning parameters of 120 kV, 15 W and exposure time 270 ms, revealing salt deposition patterns at the pore scale. A 1.5 mm aluminium filter was used for all scans to mitigate beam hardening. Images were reconstructed in 3D and subjected to an image processing pipeline in Dragonfly 3D World (v. 2024.1), as outlined in Fig. 1(b-d). Image preprocessing involved ring artifact correction (to remove circular features in the reconstructed image, arising from detector element miscalibration) and anisotropic diffusion filtering as an edge-preserving denoising technique that maintains sharp transitions between different material phases. Segmentation used a supervised machine

learning approach, and a Random Forest classifier trained to distinguish between three classes: glass beads, air, and dried salt. Manual annotations were prepared on representative 2D slices to generate the training dataset. The classifier evaluated voxel intensities and derived local features to enhance class separability. The trained model was then applied to the 3D volumes to produce segmented outputs, which were validated against manually annotated frames.

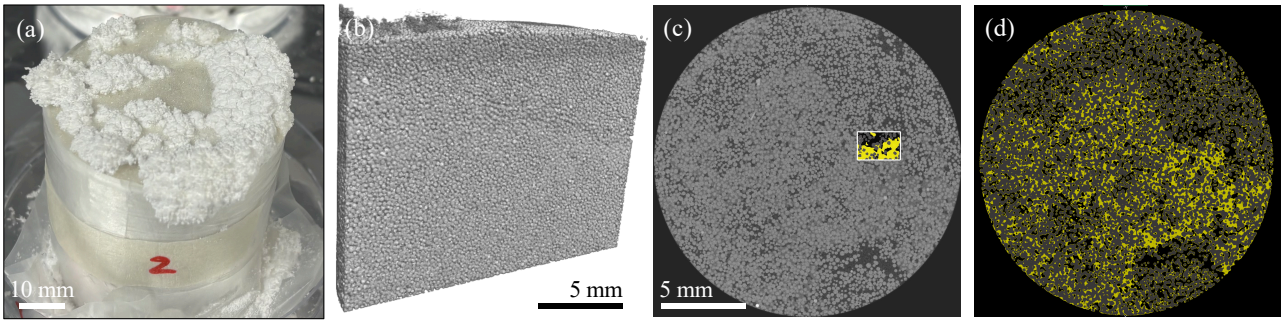

***Figure 1**: Methods of salt visualisation. (a) Fully dried specimen, contaminated by sodium sulfate, and displaying extensive surface efflorescence. (b) Transverse section of a 3D micro-CT tomogram of 10 µm resolution. (c) Horizontal slice of the same tomogram, after pre-processing, and with training region highlighted. (d) Fully processed and segmented slice, showing locations with salt (yellow), beads (grey) and air (black).*

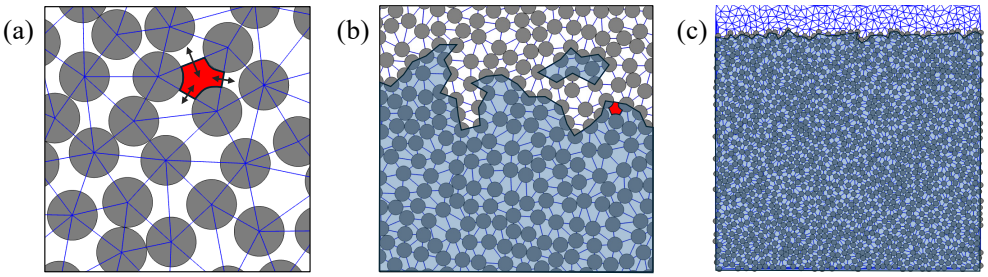

***Figure 2**: Model setup. (a) A porous stone is approximated by a set of grains. A triangulation of their centres yields a network of pores (white areas) connected by throats (blue lines). An exemplar pore (red) can exchange material (arrows) with 3 neighbours. (b) The simulation follows the evolution of the air/water interface. An invaded pore (red) releases water into all pores connected to it. (c) Initially, all pores are wet, except for a thin boundary layer of air.*

3 Pore-network model of salt transport and crystallisation

We formulate a novel pore-network model, utilising the OpenPNM framework (Gostick *et al.* 2016). Pore geometry is derived from a random packing of spherical grains in a rectangular domain, discretizing the pore space between them into a network of pores and throats (Fig. 2a). Here, a pore is defined as the open area between three neighbouring grains, and a throat as the narrowest constriction between two adjacent grains. Each pore can exchange material with three neighbours, with rates computed via constitutive rules that model mass transport by advection and diffusion, where conductance scales with the throat size (assuming laminar flow). Pores can contain either air or water (with dissolved salt), or an air-water interface (Fig. 2b). The simulations track the evolution of these phases.

We model drying as the transport of water in its vapour phase from wet pores into the environment, following Borgman *et al.* (2017). Diffusion between adjacent air-filled pores is approximated by Fick's laws, *i.e.* proportional to the local (interpore) gradient of the vapour concentration and the cross-sectional area of the connecting throat. Evaporation from each cluster of connected wet pores is the sum of the evaporative losses from all their interfacial pores. We assume a separation of timescales between rapid invasion events (Haines jumps) and slower evaporation processes. This means that, for any configuration of the air-water interface, we only solve for diffusion (calculate the matrix of diffusive fluxes) once. When a cluster has lost sufficient water to allow capillary invasion, a wet pore on its boundary is invaded by air. Invasion is treated effectively as an instantaneous, event-driven process: the fluid from the invaded pore is redistributed to all pores on the interface of the connected cluster to which it belongs, to replenish their accumulated evaporative losses. Physically, this represents the instability of a capillary meniscus in a throat, with fluid flow (interfacial readjustments) to relax all other connected menisci. The corresponding internal flows within the cluster are calculated assuming laminar (Poiseuille) flow. After each invasion event is complete, we recalculate the diffusive fluxes for the updated interface.

Between invasion events, salt transport is also diffusive, and calculated in the same manner as vapour diffusion, but on the water-filled pores. The modelling approach is based on the dissolution model of Budek and Szymczak (2012). Salt concentrates on interfacial pores to balance evaporative losses, which remove fluid volume but not salt. During invasion, salt is also redistributed advectively with the water flow. If the concentration of salt in a pore exceeds its equilibrium saturation level, then salt is precipitated out as a solid mass, and we track the location of such salt deposits over time.

The model's boundary and initial conditions (Fig. 2c) are as follows: The top boundary is open to air, with a fixed relative humidity, mimicking a well-stirred room. A region of open, air-filled model cells represents a boundary layer of stagnant air above the drying porous sample. Water with a given initial concentration of salt initially occupies the remainder of the pores, and no-flux conditions are imposed on the sidewalls and bottom. The model is implemented using rescaled variables, where the bead size is the characteristic length, and the vapour diffusion sets a characteristic timescale. It can be adapted to any real physical system by the choice of the system size (here, 20 × 20), the boundary layer thickness (here, the top 10%), and the ratio of the diffusion constants of water vapour and dissolved salt (here, taken as 20).

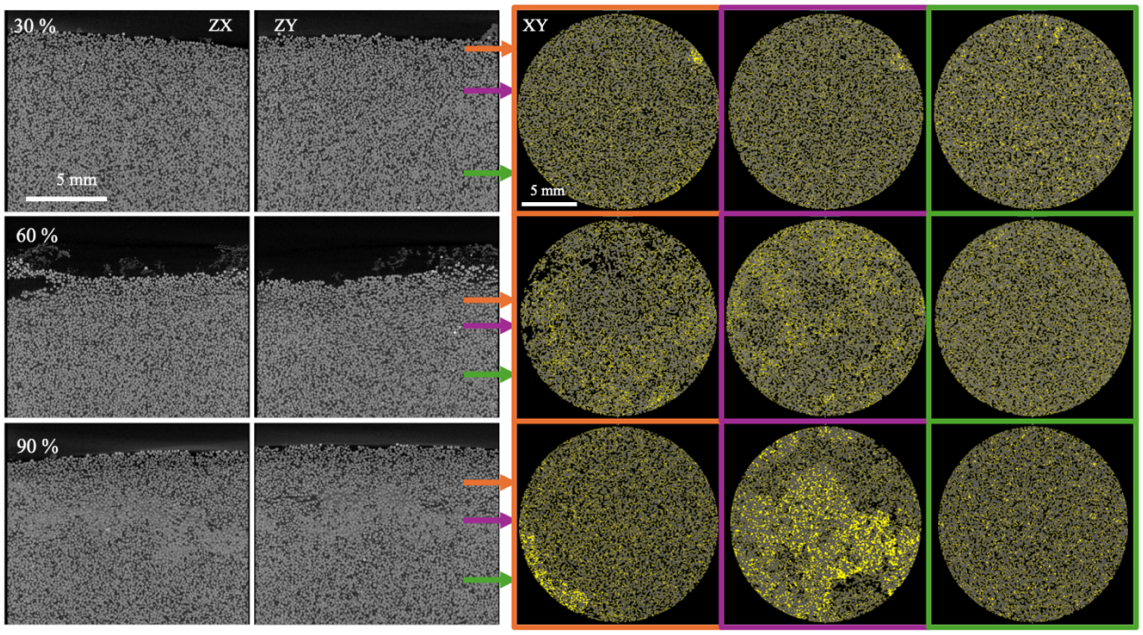

***Figure 3**: Measuring salt distributions in artificial stone specimens. Experiments involved samples initially invaded by a sodium sulfate solution of (top) 30 %, (middle) 60% and (bottom) 90% saturation. For each experiment, two orthogonal vertical slices (ZX, ZY) through the 10 µm tomogram are shown, along with three horizontal slices (XY, at depths indicated by the arrows) through the segmented data, showing salt (yellow), beads (grey) and air (black).*

4 Results

The segmentation and post-processing of the micro-CT data enable a detailed, quantitative comparison of the different phases of salt, glass beads and air. Classifications of phases in the dried specimens with different initial salt concentrations can easily highlight the spatial distribution of deposited salt, as in Fig. 3 for the 10 µm resolution scans. However, the Random Forest algorithm was found to be challenged by the bead surfaces, and voxels on air-glass boundaries were frequently misclassified as salt, due to partial volume effects and the grayscale similarity between these phases (salt is intermediate between air and glass). To correct for this, segmented data was further post-processed in Matlab, using morphological operations such as dilation and connected component analysis to reassign misclassified edge voxels, based on spatial context and the relative abundance of the different phases in the immediate neighbourhood of each voxel.

The corrected proportions of segmented voxels of the different phases (air, salt and beads) were then summed across different horizontal slices of the 3D data. Figure 4 shows how the relative composition of these phases varies with depth, and highlights clear trends correlated with the initial salt concentration. In the 30% sample, salt crystallised in small patches spread out through the entire specimen, with some modest efflorescence, due to the limited solute availability during drying. Stronger efflorescence occurred in the 60% sample (see tomograms in Fig. 3, fluffy deposits above the sample). Damage to the porous matrix is also evident, in the form of near-surface cracks. The patches of salt are larger and more concentrated near the surface, with a distinct peak in the volume of deposited salt at ~3 mm depth. Indeed, pronounced subflorescence is evident for the 60% and 90% samples, with salt fractions peaking below the evaporative surface and extending deeper into the porous matrix. The 90% sample showed the highest overall internal salt content, which is distributed across two clear peaks, near to (~1 mm depth) the evaporative surface and in the mid-volume of the sample (~5 mm depth), indicating a strong dependency between initial concentration and crystallisation pattern.

To compare the numerical simulations with the experiments, we tuned the numerical parameters so that in both cases the ratios of diffusive to evaporative effects agree (*i.e.* Péclet numbers match), using the parameters given in Section 3, and matched the initial salt concentrations to those studied experimentally. Figure 5(a-c) shows how the predicted distributions of salt vary with location, in the final, dried states of three simulations with the same pore geometry, but different initial salt concentrations. To improve the quality of the numerical predictions, we then averaged the results of 20 such

simulations, with different randomly generated geometries, to give the depth-dependent distributions of salt shown in Fig. 5(d). In general, the trends seen here agree with experimental observations–more salt is deposited, and deeper within the sample, for higher initial salt concentrations. The salt deposits are also layered, with pronounced peaks at about 1 and 2 mm depth. Finally, in the simulations we could adjust the ratio of evaporation to diffusion by our parameter choices. As an initial test along this direction, we found that enhancing evaporation rates by *e.g.* a factor of 10 led to a pronounced shift of the dried salt deposit towards the drying surface.

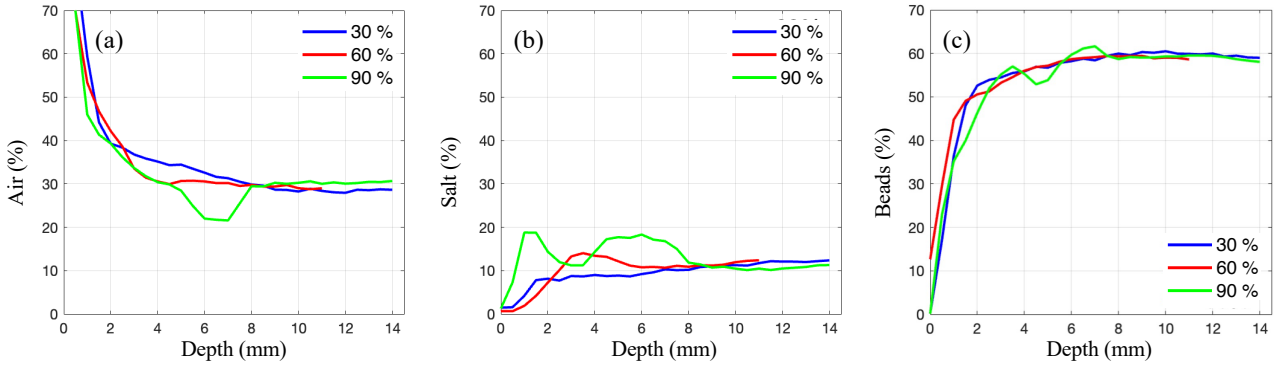

***Figure 4**: The fractions of voxels categorised as (a) air, (b) salt and (c) glass beads were measured from the segmented data, and horizontal slices extracted at different depths from the evaporating surface. Results are shown for specimens initially filled with sodium sulfate solutions at 30% (blue), 60% (red) and 90% (green) of saturation.*

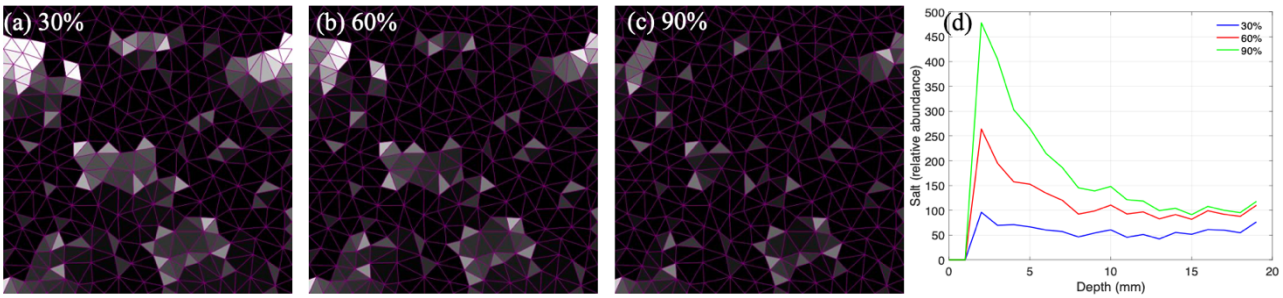

***Figure 5**: Salt distributions in the pore-network model. The final, dried state is shown for simulations with identical pore geometry, initially filled with fluid at (a) 30%, (b) 60% and (c) 90% of the salt saturation concentration. The brightness of each pore (triangle) is proportional to the amount of salt deposited. (d) Salt deposition versus depth is calculated from an ensemble of 20 independent simulations, each with a different pore microstructure.*

5 Conclusions

The precipitation patterns observed in this study generally agree with previous findings on salt behaviour in porous media. For instance, Nunes *et al.* (2021) and Flatt *et al.* (2017) emphasise the role of initial salt concentration and moisture gradient in dictating crystallization mechanisms. Similarly, Li *et al.* (2024) highlight the decisive roles of evaporation rates and capillary action on the shape of salt distribution patterns. This agreement supports our observations of enhanced efflorescence in samples with lower brine concentrations, *vs.* more significant subflorescence at higher salt concentrations. It also validates our approach of relying on simplified settings (artificial sandstone, enhanced drying) to mimic real scenarios. In terms of image processing protocol adopted for this research, our post-processing also reflects the recommendations of the Analytical Methods Committee (2021), which highlights the interdependence of sample size and scanning resolution (voxel size) and their effect on segmentation accuracy and voxel classification when interpreting micro-CT data of stone and related materials. The integration of supervised machine learning with morphological post-processing corrections also shows good potential to address common issues of phase misclassification at interfaces (such as air-bead edges) due to overlapping of X-ray attenuation characteristics. This can enhance the reliability of voxel classification, and hence the accuracy of phase analysis throughout different regions of interest in the sample.

The presented analyses were based on high-resolution (10 µm) micro-CT scans on sub-samples, acquired near the specimen surface. Future work will also elaborate and apply the segmentation protocol (from machine learning to post-processing) to full micro-CT volumes captured at lower resolution (30 µm), and to more diverse specimens. This approach will enable analysis of larger volumes of substrates and enhance identification of large-scale heterogeneities and crystallization fronts. We also plan to conduct comparative studies across different real heritage samples, like sandstones, to validate the experimental workflow and segmentation protocol in more complex and realistic systems. The insights gathered from this extended study will then better serve as a foundation for refining the computational models for salt

transport and crystallization dynamics in heritage materials. In particular, through this approach we aim to explicitly include the feedback between salt precipitation and transport, with salt deposits clogging or limiting movement. In this way, the results shown here are aimed at developing a more robust investigation pipeline for predicting salt dynamics.

Acknowledgements

This project has received funding from the European Union's Horizon Europe research and innovation programme under grant agreement No 101131765 (EXCITE2) for Transnational Access conducted at UPPA-DMEX-FRANCE. Additional microscopy facilities, including image analysis support, were provided by the Imaging Suite at the School of Science and Technology at NTU; we thank Graham Hickman for his support. MC, NH and RH acknowledge support from the Engineering and Physical Sciences Research Council (EP/V050613/1). HD acknowledges the support from the ERC Starting Grant PRD-Trigger (grant agreement N° 850853).

References

Analytical Methods Committee AMCTB No. 109, 2021, X-ray micro-computed tomography for heritage building materials, Anal. Methods, 13, 5875.

Borgman, O., Fantinel., P., Lühder, W., Goehring, L., and Holtzman, R., 2017, Impact of spatially correlated pore-scale heterogeneity on drying porous media, Water Resour. Res., 53, 5645–5658.

Budek, A., and Szymczak, P., 2012, Network models of dissolution of porous media, Phys. Rev. E, 86, 056318.

Flatt, R.J., Caruso, F., Sanchez, A.M.A., and Scherer, G.W., 2014, Chemomechanics of salt damage in stone, Nat. Commun., 5, 4823.

Flatt, R.J., *et al.*, 2017, Predicting salt damage in practice: a theoretical insight into laboratory tests, RILEM Technical Letters, 2, 108-118.

Godts, S., et al., 2022, Modeling salt behavior with ECOS/RUNSALT: Terminology, methodology, limitations, and solutions, Heritage, 5, 3648-3663.

Godts., S., et al., 2024, Modeled versus experimental salt mixture behavior under variable humidity, ACS Omega, 9(18), 20454-20466.

Gostick, J., *et al.*, 2016, OpenPNM: a pore network modeling package, Comput. Sci. Eng., 18(4), 60-74.

Kogou, S., *et al.*, 2025, Ground-based remote sensing and machine learning for in-situ and noninvasive monitoring and identification of salts and moisture in historic buildings, Anal. Chem., 97, 5008−5013.

Hemmerle, A., Schröter, M., and Goehring, L., 2016, A cohesive granular material with tunable elasticity, Sci. Rep., 6, 35650.

Li, Q. *et al.*, 2024, A perspective view of salt crystallization from solution in porous media: morphology, mechanism, and salt efflorescence, Sci. Rep. 14, 23510.

Menéndez, B., 2017, Estimation of salt mixture damage on built cultural heritage from environmental conditions using ECOS-RUNSALT model, J. Cultural Heritage 24, 22–30.

Miletić, M. Küçükuysal, C., Gülcan M., and Garcia, R., 2024, Imaging porosity evolution of tight sandstone during spontaneous water imbibition by X-ray Micro-CT, Heliyon, 10, e31844.

Noriel, C., and Soulaine, C., 2021, Pore-scale imaging and modelling of reactive flow in evolving porous media: tracking the dynamics of the fluid–rock interface, Trans. Porous Media, 140, 181-213.

Nunes, C., *et al.*, 2021, Experimental research on salt contamination procedures and methods for assessment of the salt distribution, Constr. Build. Mater., 298, 123862.

Reedy, C.L. and Reedy, C., 2022, High-resolution micro-CT with 3D image analysis for porosity characterization of historic bricks, Heritage Sci., 10, 83.

Seigneur, N., Mayer, K.U., and Steefel, C.I., 2019, Reactive transport in evolving porous media, Rev. Mineral. Geochem., 85, 197-238.

Wetzei, M., Kempka, T., and Kühn, M., 2020, Hydraulic and mechanical impacts of pore space alterations within a sandstone quantified by a flow velocity-dependent precipitation approach, Materials, 13, 3100.

Zhao, B., *et al*. 2019, Comprehensive comparison of pore-scale models for multiphase flow in porous media, Proc. Nat. Acad. Sci., 116(28), 13799-13806.